Polymer Composites

WILEY | spe INSPIRING PLASTICS PROFESSIONALS

RESEARCH ARTICLE OPEN ACCESS

Nanoparticles Dispersion Assessment by a Novel Pulsed Laser-Induced Micro Thermography Technique

Nicola Montinaro[1,2] | Guglielmo Marchesa[1] | Donatella Cerniglia[1] | Antonio Pantano[1]

[1]Department of Engineering, Università degli Studi di Palermo, Palermo, Italy | [2]National Institute for Astrophysics (INAF), Osservatorio Astronomico di Palermo, Palermo, Italy

Correspondence: Nicola Montinaro (nicola.montinaro@unipa.it)

Received: 30 January 2025 | **Revised:** 1 May 2025 | **Accepted:** 24 May 2025

Funding: The authors received no specific funding for this work.

Keywords: aggregate | dispersions | laser thermography | microstructure | nanocomposites | NDT

ABSTRACT

This work wants to propose an innovative nondestructive pulsed thermographic approach utilizing a nanosecond pulsed laser as a heat source for assessing the presence of nanoparticles aggregates in nanocomposites. Different degrees of dispersion levels of carbon nanotubes (CNTs) enriched epoxy resin nanocomposites were investigated with a cooled infrared camera equipped with a macro lens to improve the geometric resolution of the images (up to 6 μm). The technique successfully exploits the concentrated energy flux delivered by the laser in a short time, allowing for a significant improvement in energetic resolution. CNTs clusters with sizes as low as 6.8 μm were identified by image analysis algorithms as embedded in the matrix with well-defined contours. This research represents a significant advancement in image quality and time reduction for fast non-destructive evaluations (NDE) in the field of nanocomposites. In turn, the process is suitable for automated in-line quality control of manufactured parts that must meet desired specifications.

1 | Introduction

Carbon-based polymeric nanocomposites (NCs) combine the low cost and ease of processability of polymeric matrices, either thermoplastic or thermosetting, with the high-performance properties of carbon nanostructures, such as carbon nanotubes, nanoplates, and graphene. Thanks to their exceptionally high specific surface area, even the addition of small amounts of nanofiller into the polymer can impart desirable functional and mechanical properties to the material. The enhancement of electrical and thermal conductivity [1, 2], as well as mechanical properties, such as ultimate tensile strength, stiffness, hardness, wear resistance, and fatigue life [3, 4] is nowadays well documented.

However, to fully exploit the valuables of carbon-based NCs, a good dispersion and homogeneity of the nanofillers in the polymer must be achieved. It is well known that nanoparticles (NPs) strongly tend to self-aggregate [5]. This could lead to large clusters within the matrix that strongly inhibit the potential performance enhancement of the nanostructured material [6]. Up to now, the prime methods for assessing the NPs dispersion level in NCs are transmission electron microscopy (TEM) and scanning electron microscopy (SEM). Both techniques can acquire extremely high-resolution images but suffer from a very localized area of inspection, which hardly can give overall information about large specimens, being time and cost demanding too [7, 8]. Also, special attention to sample preparation is needed before inspection (cut, clean etc.). On the contrary, industrial applications must involve a method for quality control that is statistically reliable and that does not damage the material. Therefore, a branch of the current research focuses on quick and easy non-destructive evaluation (NDE) techniques to assess the dispersion level of NPs into NCs. For instance, impulse acoustic

Summary

- A non-destructive pulsed-laser excited thermography technique is proposed.
- The dispersion level of CNTs into epoxy nanocomposites is evaluated.
- New upper limit for image resolution and time efficiency in laser-induced thermography.
- The approach promises automated in-line quality control of filled nanocomposites.

microscopy was successfully employed to evaluate the filler distribution in graphene NCs [9]. Also, acoustic microscopy has been employed coupled with synchrotron X-ray microtomography for the study of the microstructure in carbon-based polymer composites [10]. In addition, rapid NP dispersion assessment in nanomaterials has been conducted with non-linear ultrasonic testing [11]. Dynamic scanning calorimetry (DSC) is another possible method that was used to estimate the carbon nanotubes homogeneity in the NC by analyzing the exothermic reaction during the hardening cycle of the matrix [12]. Additional through-the-curing-process NPs dispersion assessment methods include rheological-based techniques [13, 14].

Among NDEs, infrared thermography (IRT) is standing out as a powerful technique being distinguished by fast, non-contact, and remote part inspections and characterization. In particular, the technique is based on the different thermal responses between the matrix and the filler after being subjected to a heat stimulus. Different thermal properties within the phases present in the material's volume can affect the temperature fields in the material, with consequent changes and irregularities in the infrared emission at the material's surface. This can then be analyzed using a sequence of frame images recorded by an IR camera.

In active IRT, the type of heat source used to generate the thermal front discriminates the technique. In pulsed thermography (PT), a flash lamp surface irradiation allows the generation of a packet of heat waves with different amplitudes and frequencies that propagate inside the medium in a transient mode.

In modulated frequency thermography, a halogen lamp is used instead of a flash, where the deposition of the heat is modulated by switching on and off a lamp at a fixed rate [15, 16].

However, the use of a halogen lamp as a heating source in the IR thermography technique has some drawbacks, such as inhomogeneous heating along the sample surface and the need to protect the camera from the light source through shielding apparatus [17]. An alternative and more flexible heating source for pulsed thermography applications is the pulsed-laser source. Pulsed laser excitation has been employed in thermography techniques for non-destructive and thermophysical properties investigation in composites [18–20]. This setup allows for higher sensitivity and enhances thermal contrast, but the constrained spot of the focused laser beam limits the size of the investigated area achievable [21]. However, today the robotization of inspection techniques, which adopt the IR method combined with a robotized manipulator and a laser source as an end effector, would allow for rapid analysis of large and complex-shaped areas [22–25]. Robotic inspection has become commonplace due to research investments from the aerospace sector focused on the effectiveness of ultrasonic techniques for inspecting critical components. Additionally, automated geometry mapping has been demonstrated using robotically manipulated metrology sensors [26]. Although a thermographic setup in reflection mode, featuring a laser heat excitation source and an IR camera positioned on the same side of the component under inspection, is not ideal for examining deep within the volume of a part, it offers the benefits of being contactless and full-field, meaning it provides information on the entire IR camera field of view (FOV) remotely all at once. The robotic manipulation of thermographic instrumentation enables industrial quality inspections of large components with intricate geometries by capturing multiple thermographic images at designated positions.

As previously highlighted, thermography NDE techniques have recently been successfully employed in NCs quality control. Specifically, infrared micro-thermography (IRMT) allowed for void and thermal diffusivity mapping of graphene-based NCs, from $1\%_{wt}$ to $10\%_{wt}$, with a resolution of 200 μm/pxs and 100 μm/pxs, respectively [27, 28]. The IRMT setup is also adopted for NPs dispersion assessment. For instance, lock-in thermography was used to detect and quantify small percentage of Au NPs embedded in thin polymeric films [29]. Also, graphite and graphene-based NCs manufactured by batch, planetary, and hand mixing, were compared in relation to the level of dispersion using micro-IRT coupled with machine learning models with a resolution of 20 μm/pxs [30, 31]. Again, the thermal response in IRT of multi-wall CNTs NCs highlighted how samples with higher order of NPs distribution had a greater sensitivity to the heat wave, thus rising in temperature in a shorter time [32]. Finally, pulsed phase thermography (PPT) allowed for cluster detection with a resolution as low as 21 μm/pxs of both nano-Ag filled Polypropylene [33] and epoxy-CNTs NCs [34]. This work proposes a novel laser-based micro-thermography technique for assessing NP dispersion in NCs. It aims to merge two existing techniques used in thermography analysis: laser-induced thermography and pulsed thermography, alongside micro-thermography. By combining these methods, we aim to take advantage of both approaches to enhance the energy and geometric resolution for evaluating the dispersion levels of NPs in NCs. The novel approach is here called pulsed laser micro-thermography (PLMT) and is tested on benchmark epoxy samples enriched with CNTs with different grades of particle dispersion. The outcomes are beneficial for in situ inspection during the production of nanostructures, enabling rapid quality control of manufactured components and maximizing the full potential of the materials.

2 | Materials and Methods

2.1 | Sample Manufacturing

The benchmark NCs samples are manufactured by enriching epoxy resin (SX10 resin by *Mike Compositi, Milan, Italy*) with $0.5\%_{wt}$ and $1\%_{wt}$ of carboxylated functionalized carbon nanotubes (COOH-CNTs procured by Cheap Tubes Inc., Grafton, VT, USA) see Table 1 for specifications.

TABLE 1 | Specifications of the materials employed for nanocomposites manufacturing.

Epoxy	
Product name	SX 10 EVO
Type	Bisphenol A modified Epoxy resin
Viscosity@ 25°C	1200 ± 250 mPas
Specific weight	1.1/1.15 g/cm^3
Hardener	
Product name	SX 10 EVO
Type	Modified cycloaliphatic polyamine
Viscosity@ 25°C	30 ± 10 mPas
Specific weight	0.95 ± 0.05 g/cm^3
CNTs	
Type	COOH Functionalized MWCNTs
Outer diameter	30-50 nm
Length	10–20 m
Purity	> 99.9%$_{wt}$
True density	2.1 g/cm^3

Two distinct processes were developed, optimized, and compared for effectively dispersing NPs into resin. Each process included one or more dispersion steps, which involved a combination of magnetic stirring at ambient temperature (350 rpm for 15 min) followed by bath sonication (150 W at 60°C for 60 min). The main difference between the two processes is the adoption of acetone as a diluting dispersing agent. These processes will be from now on referred to as Process A and Process B, respectively.

In Process A, NPs were first added to acetone and subjected to the dispersion step. Once the NPs were adequately dispersed, the resin was added to the solution at a ratio of 20%$_{wt}$ (solvent/resin) and processed again with the dispersion step. Hermetically sealed containers were used to prevent solvent evaporation. Finally, the acetone was removed by placing the solution under vacuum (5 kPa at 80°C for 90 min). In contrast, Process B involved only one dispersion step and did not include acetone removal. This significant difference influenced both the processing time and the dispersion quality of the NCs. In Figure 1, a process workflow schematization is provided for clarity.

The hardener was mixed into the enriched resin by hand using a rigid plastic stick. The resulting solution was then poured into flexible molds made of 3D-printed thermoplastic polyurethane, which had been previously coated with a 10%$_{wt}$ PolyVinyl Alcohol solution to act as a releasing agent. The specimens were cured for 8 h at 25°C, followed by a post-curing process at 60°C for 24 h, as recommended by the resin supplier. Subsequently, both surfaces of the samples were machined using a milling machine and then sanded with 200 and 400 grit sandpaper. Finally, the samples were cleaned with acetone. Additionally, a control sample of pure epoxy was manufactured using the same molds, hardening cycle, and post-processing steps as the NCs, resulting in a total of five samples sized 40 × 40 × 3 mm^3 (See Figure 2).

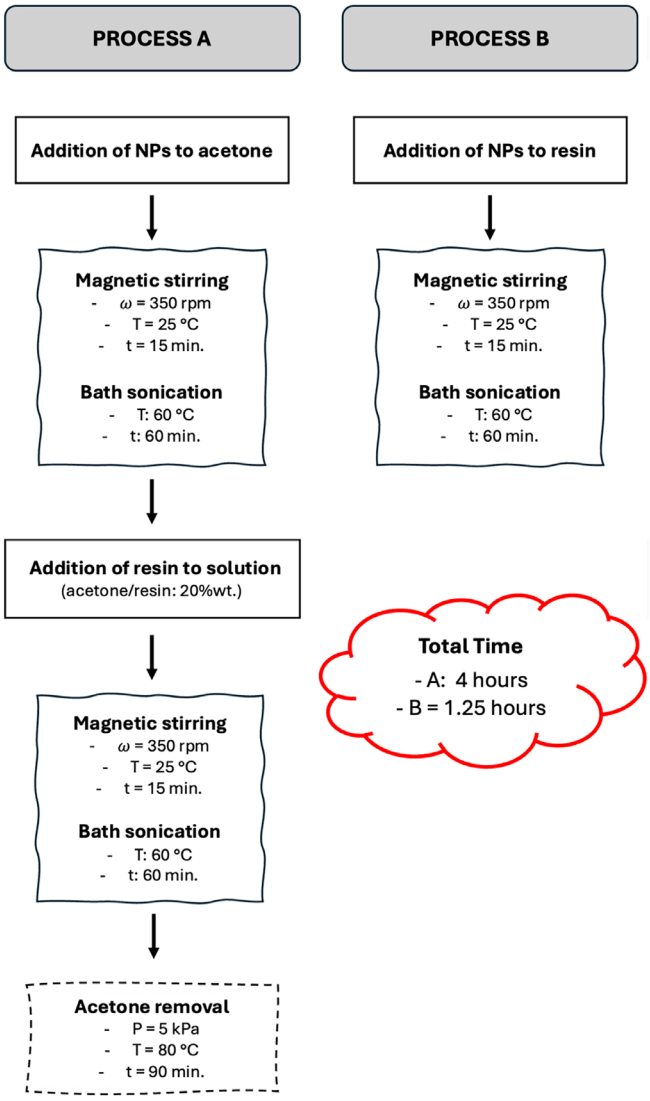

FIGURE 1 | Schematic block diagram of the CNTs manufacturing process A and process B.

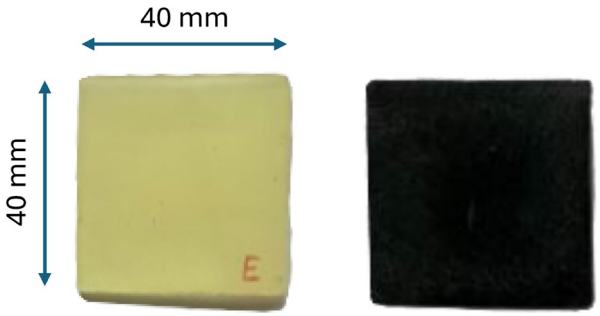

FIGURE 2 | Pure epoxy resin sample (on the left) and, 0.5%$_{wt}$ CNTs-epoxy nanocomposite sample (on the right).

The same sample was used in the degradation assessment to set the maximum pulsed injectable energy. Thermal parameters for COOH-CNTs in bundles, cured epoxy resin, and air are reported in Table 2. It is well known in the literature that ideal dispersion and separation of NPs would lead to even higher thermal conductivity values [5, 31], but this is hard to obtain. Before conducting the thermographic inspection, SEM images

of NC samples were acquired to examine the dispersion levels coming from processes A and B. In process A, which used acetone as a diluting agent along with prolonged stirring and sonication, as expected a higher level of NP dispersion was achieved. The aggregates of CNTs generally maintained the same dimensions, averaging between 10 and 20 μm. In contrast, the samples obtained through process B exhibited larger aggregates, with sizes ranging from 20 to 200 μm, leading to increased scattering (Figure 3). The samples coming from the process A and B are here on called Sample A and B respectively.

2.2 | Pulsed Laser Micro-Thermography (PLMT) Experimental Setup

Non-destructive analyses were performed with an innovative PLMT technique in reflection mode. The experimental setup comprises a pulsed laser made by Quantel (Quantel laser, Lumibird group, Lannion, FRANCE), model Brilliant B, whose beam is focused on the sample surface utilizing optics for the beam path, spherical lens to focus on the sample surface, and an IR-camera to acquire the thermal footprint. The adopted IR-camera is a FLIR X6540sc (FLIR Systems, Wilsonville, OR, USA) with a cooled indium antimonide (InSb) sensor (640 × 512 pxs), armed with a MW G1 F/3.0 macro lens of the same manufacturer, eventually equipped with two extension rings with 12 and 18 mm in spacing distance. The extension rings allow for increased spatial resolution and magnification (respectively from 15 to 6 μm/px) at the cost of a reduced stand-off distance (from 300 to 287 mm), and FOV (from 9600 to 3840 μm in horizontal). A schematic representation of the PLMT setup is shown in Figure 4a, while the main experimental setup parameters are detailed in Table 3.

TABLE 2 | Thermal properties for epoxy resin [35], air [36], and bundled CNTs [37].

Property	Epoxy resin	Air	Bundle CNTs
Thermal conductivity (l) [W/m K]	0.35	0.026	150
Specific Heat (c_p) [J/Kg K]	$0.3*10^3$	$1*10^3$	$0.75*10^3$
Density (ρ) [g/m^3]	$1.15*10^3$	1.2	$2.6*10^3$
Thermal diffusivity (α) [m^2/s]	$0.1*10^{-5}$	$2.2*10^{-5}$	$7.7*10^{-5}$

Figure 4b,c show the dimension comparison between the camera FOV, the laser spot, and the sample size for the setup with and without the extension ring on the IR camera. The thermal field is generated by the nanosecond pulsed far-infrared laser operating at 1064 nm whose power can be tuned by adjusting the Q-switch. The spatial energy distribution and the size of the incident beam (stated by the manufacturer as Gaussian) were experimentally validated by measuring, without the extension ring, a representative thermogram of a pulse (see Figure 5).

It is worth noting that the pulse energy deployed by the laser is a nonlinear function of the Q-switch delay that can only be set in discrete steps. For this reason, a uniform energy spacing cannot be achieved in all the desired power ranges. The irreversible damage caused in polymeric materials by the excessive localized heat enforced by high-energy sources such as lasers is a well-documented topic [38, 39]. For this reason, a preliminary assessment study was conducted on the reference pure epoxy sample to investigate the effects of laser energy pulses on material degradation. Due to the laser pulse

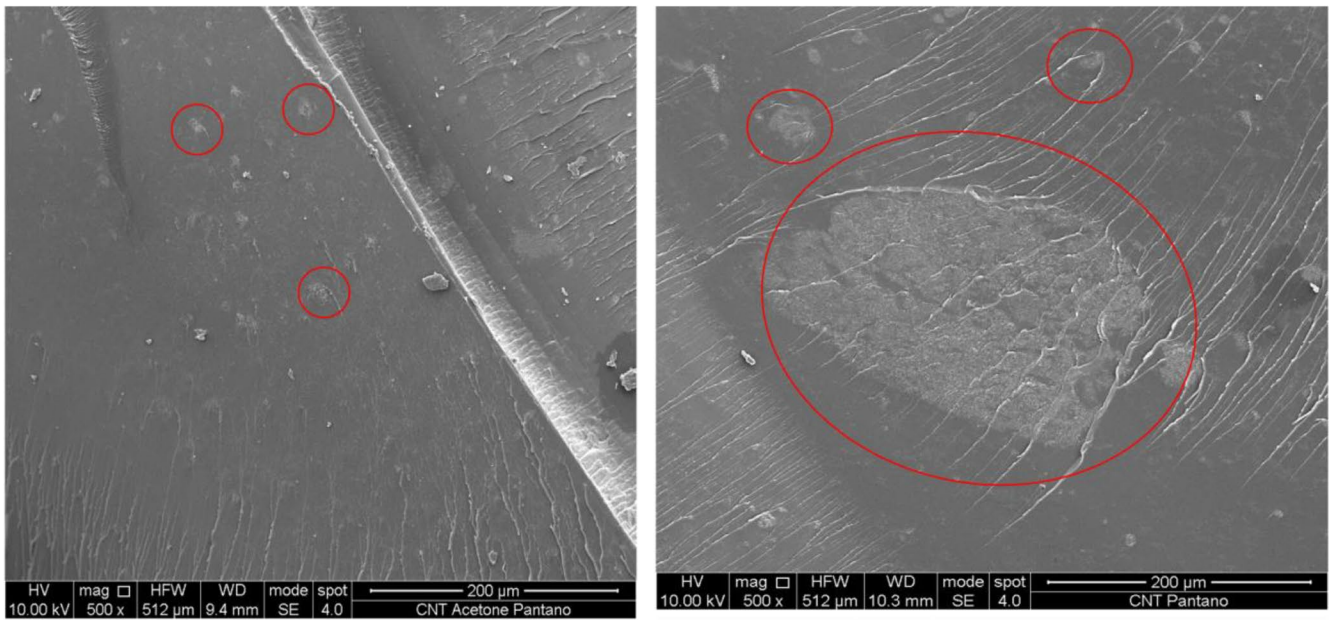

FIGURE 3 | SEM images of the manufactured CNTs-epoxy nanocomposites obtained by process A (on the left panel), and process B (on the right panel). Red circles highlight the presence of CNTs clusters.

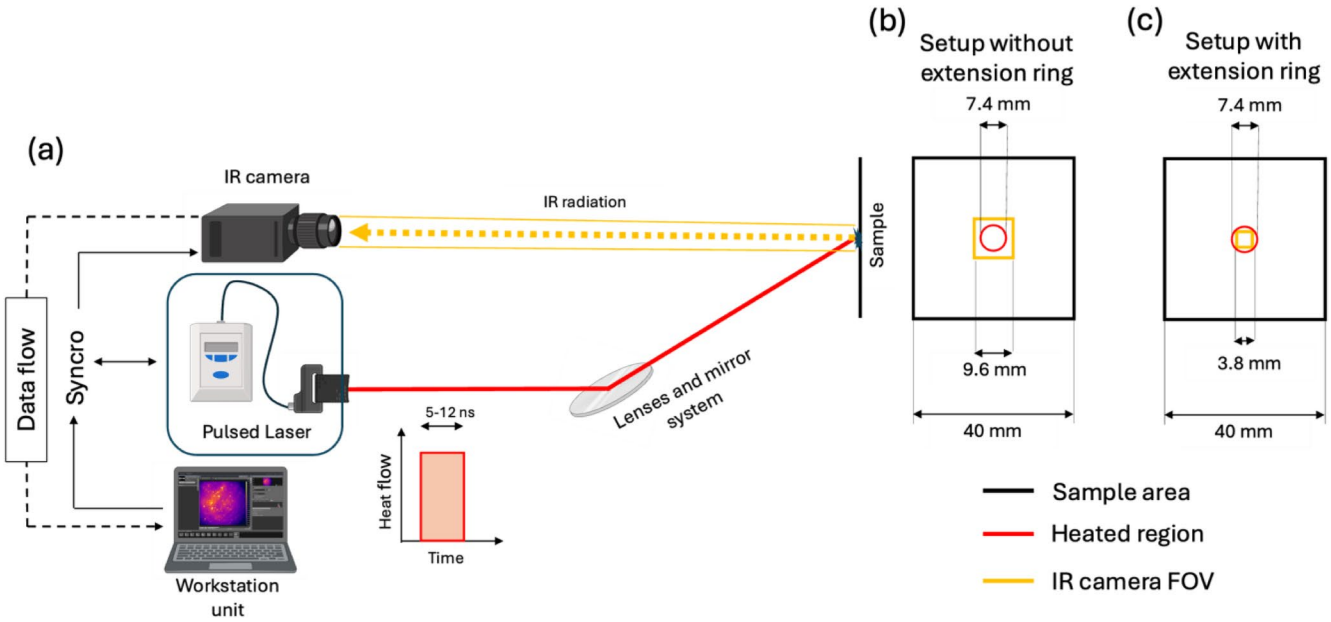

FIGURE 4 | Schematic representation of the PLMT experimental set-up without extension rings (a); dimensions of camera FOV, Laser spot, and Sample size for the setup without (b) and with (c) extension ring.

TABLE 3 | Pulsed laser micro-thermographic approach set-up parameters.

PLMT set up parameters	
Laser pulse energy range (mJ)	850–60
Pulse duration (ns)	5–12
IR-camera to sample minimum distance (mm)	287
Diameter of the laser spot on sample surface (mm)	7.4
IR-camera horizontal field of view (mm)	3.84–9.6
Time delay between shot and acquisition (μs)	10
IR-camera Integration time (μs)	2500

duration being in the nanoseconds range, special attention was given to synchronizing the infrared camera and the laser pulse to enhance the thermal contrast of the acquired thermograms. In this regard, it was experimentally observed that a perfect synchronization between the laser shot and the thermogram acquisition is not an optimal choice. This is likely due to the micro-vaporization of debris on the sample surface, generating a plume that shields the FOV of the IR camera and creates artifacts. To achieve accurate results, it is then essential to properly set the time delay of the infrared acquisition concerning the laser irradiation. Preliminary studies have determined an optimal time delay of 10 μs. To gather the particle dispersion assessment with the proposed PLMT technique, a single laser shot for each scanned area is sufficient.

A Pulsed Thermography analysis in reflection mode was conducted on the same NCs for comparison. In the PT setup, the adopted heat source is an Elinchrom Flash lamp, delivering a pulse of 4800 W*s, powered by two Elinchrom 2400 rx units in

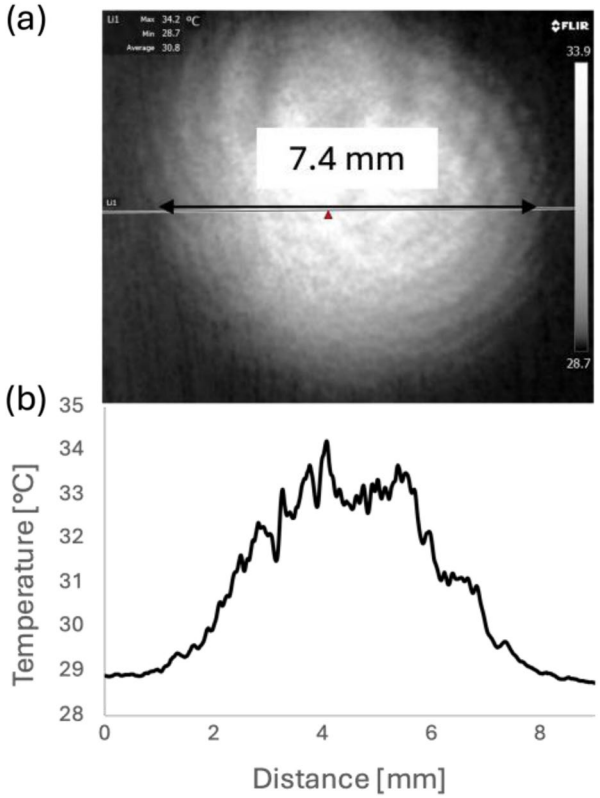

FIGURE 5 | Thermogram of a laser shot used for size and energy distribution calculation (a); temperature profile acquired along the shot diameter (b).

parallel configuration. The IR camera, equipped with extension rings, captures the temperature evolution at a 20 Hz framerate during the cooling transient after the flash pulse until the temperature becomes uniform. A schematic representation of the PT setup is shown in Figure 6, while the main experimental setup parameters are detailed in Table 4.

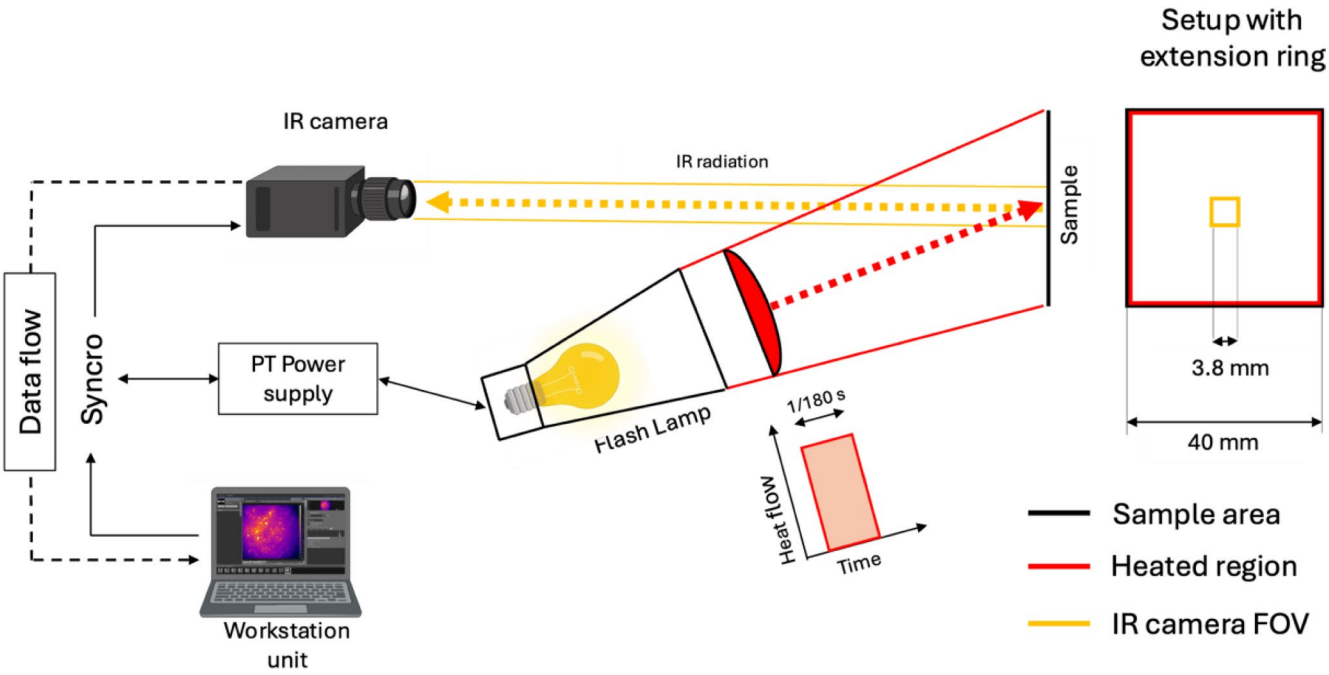

FIGURE 6 | Schematic representation of the PT experimental set-up.

TABLE 4 | PT setup parameters.

Pulsed thermography setup	
Set-up mode	Reflection
Sample-flash distance (mm)	200
Flash power (W*s)	4800
Flash duration (s)	1/180
IR camera integration time (μs)	2500
IR camera sample rate (Hz)	20
Truncation windows (s)	5

3 | Results

3.1 | Surface Degradation Study

It is well known that the polymeric matrix of NCs is prone to degrade at high temperatures. Since in the proposed technique a laser source is used to heat the specimen, an assessment of the energy density threshold beyond which the polymer would be permanently damaged is necessary and recommended. The thermal diffusivity of a material:

$$a = \frac{\lambda}{\rho c_p}$$

with λ the thermal conductivity, ρ the density, and c_p the specific heat capacity, indicates how it would react to the heat pulse. In particular, the presence of CNTs in a polymer matrix, with orders of magnitude higher thermal conductivity with respect to the resin (see Table 2) would promote heat dissipation, thus decreasing the risk of damage. To confirm the assumption, it was experimentally observed that the laser spot cooling transient on enriched samples is faster than in pure resin ones. In PLMT, a single shot is sufficient to gather information on the aggregates' dispersion; thus, it was deemed reasonable to apply a pass/fail criterion for the injected power to discriminate the surface degradation. In particular, polymer degradation is assessed by deploying progressively higher energy pulses (ranging from 112 to 317 mJ) in sets of 20 to the pure epoxy sample surface (the more prone to degradation). The sets of 20 pulses are fired on the same spot with a frequency of 2 Hz (the minimum pulse repetition rate of the laser) at a selected energy level. It must be considered that the cooling transient of the material is slower than the period of the pulse repetition rate (see Figure 12). At the end of each set, the laser focus is moved to a new pristine area, and the test is repeated with another energy level. It was experimentally observed that no damage occurred on the sample for pulsed energy below 150 mJ. Figure 7 shows the last thermographic images at the end of each set for a selected energy level. Figure 8a shows a picture of the sample fired with a set of 20 pulses below 150 mJ, while in Figure 8b the energy is above that threshold.

3.2 | NPs Dispersion Assessment

NCs containing $0.5\%_{wt}$ and $1\%_{wt}$ COOH-CNTs embedded in epoxy resin are used as a benchmark for the proposed PLMT technique. Two specimens, at $0.5\%_{wt}$ and $1\%_{wt}$ for each type, A and B, with different dispersion levels have been tested. The experiments were conducted at different magnifications adopting extension rings on the lens. Specifically, single frames were acquired after the laser pulse with a fixed time delay set to 10 μs for 5 different regions of the sample. The laser pulse energy was kept constant at 112 mJ (445 μs Q-switch) to avoid degradation, according to the previously mentioned surface degradation study (see Section 3.1). The captured thermograms are post-processed with a non-linear image processing algorithm to enhance the contrast, thus revealing the features to the operator.

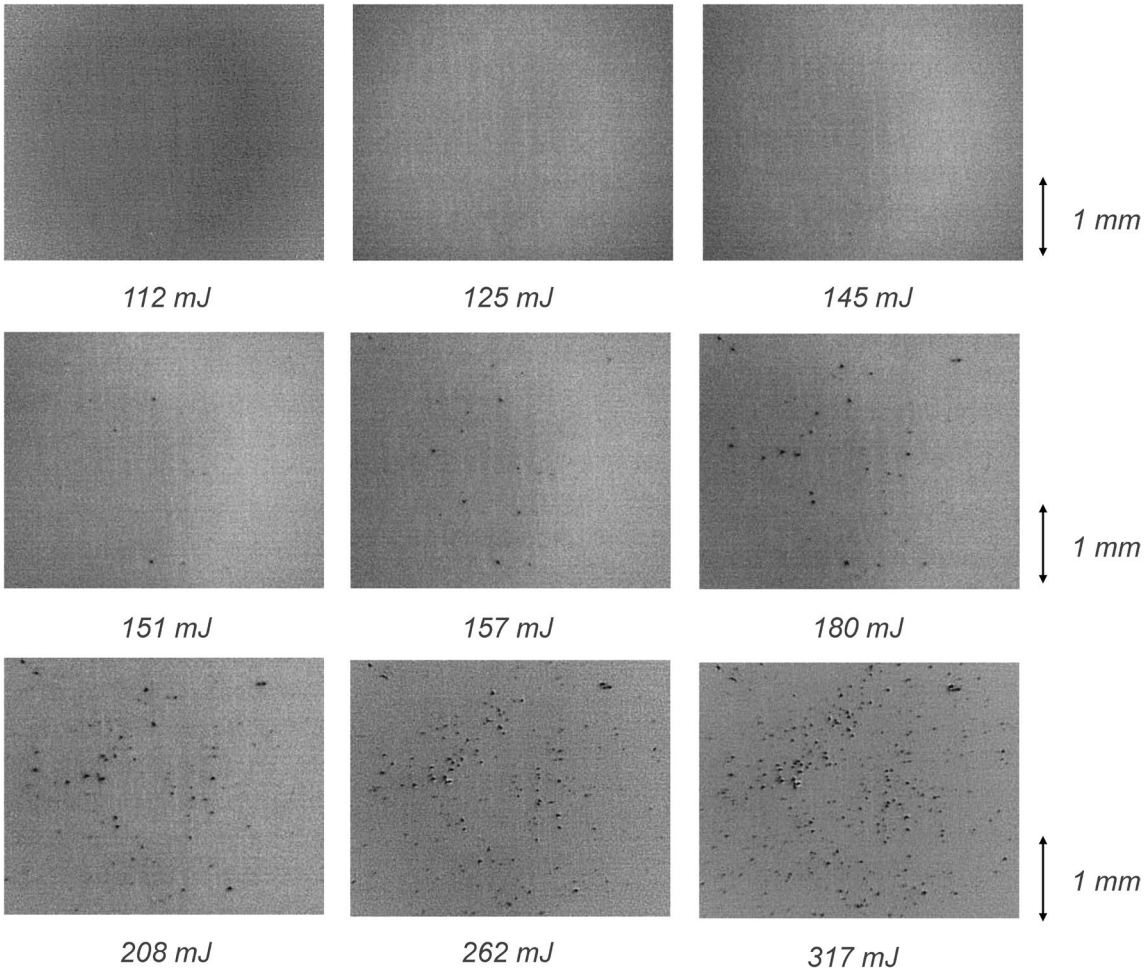

FIGURE 7 | PLMT damage assessment applied to pure epoxy resin sample.

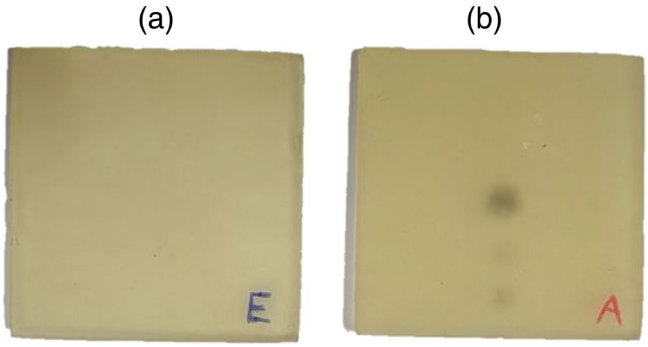

FIGURE 8 | Epoxy resin samples fired with a set of 20 pulses below 150 mJ (a) and above 150 mJ (b) in discrete spots.

In particular, the algorithm preserves the information captured on the boundary of the IR camera exposition time (see also integration time) due to the temperature dynamic of the laser pulse. Figure 9 shows the outcomes of the PLMT inspection applied to NCs coming from processes A and B with two magnification levels (Figure 9a,b without extension rings; Figure 9c,d with extension rings). The NPs aggregates are spotted in Figure 9b,d for sample B with a lower dispersion level. A better dispersion of NPs with fewer and smaller aggregates is shown in Figure 9a,c for sample A with enhanced dispersion, as expected. The average dimensions of the aggregates in sample B are consistent with those found in the SEM images of Figure 3 (of about 200 μm).

3.3 | PT and PLMT Comparison

Pulsed thermography with a more conventional setup using a pulsed lamp has been applied to Sample B for a comparison. Similarly to the PLMT methodology, five different spots were examined. In Figure 10, a comparison of the thermogram captured at the same region of sample B with the two techniques is shown. Both images are post-processed with the same algorithm enhancing the image contrast.

3.4 | Image Analysis

The acquired IR thermograms, sub-framed to a region of interest (ROI) of 2.7 mm × 2.7 mm, have been processed with ImageJ software (Open-source image processing program developed at the National Institutes of Health and the Laboratory for Optical and Computational Instrumentation LOCI, University of Wisconsin), applying integrated algorithms to determine the number of particles, together with related dimensions and positions in the images. The Sauvola auto-local-threshold method [40], specifically useful for

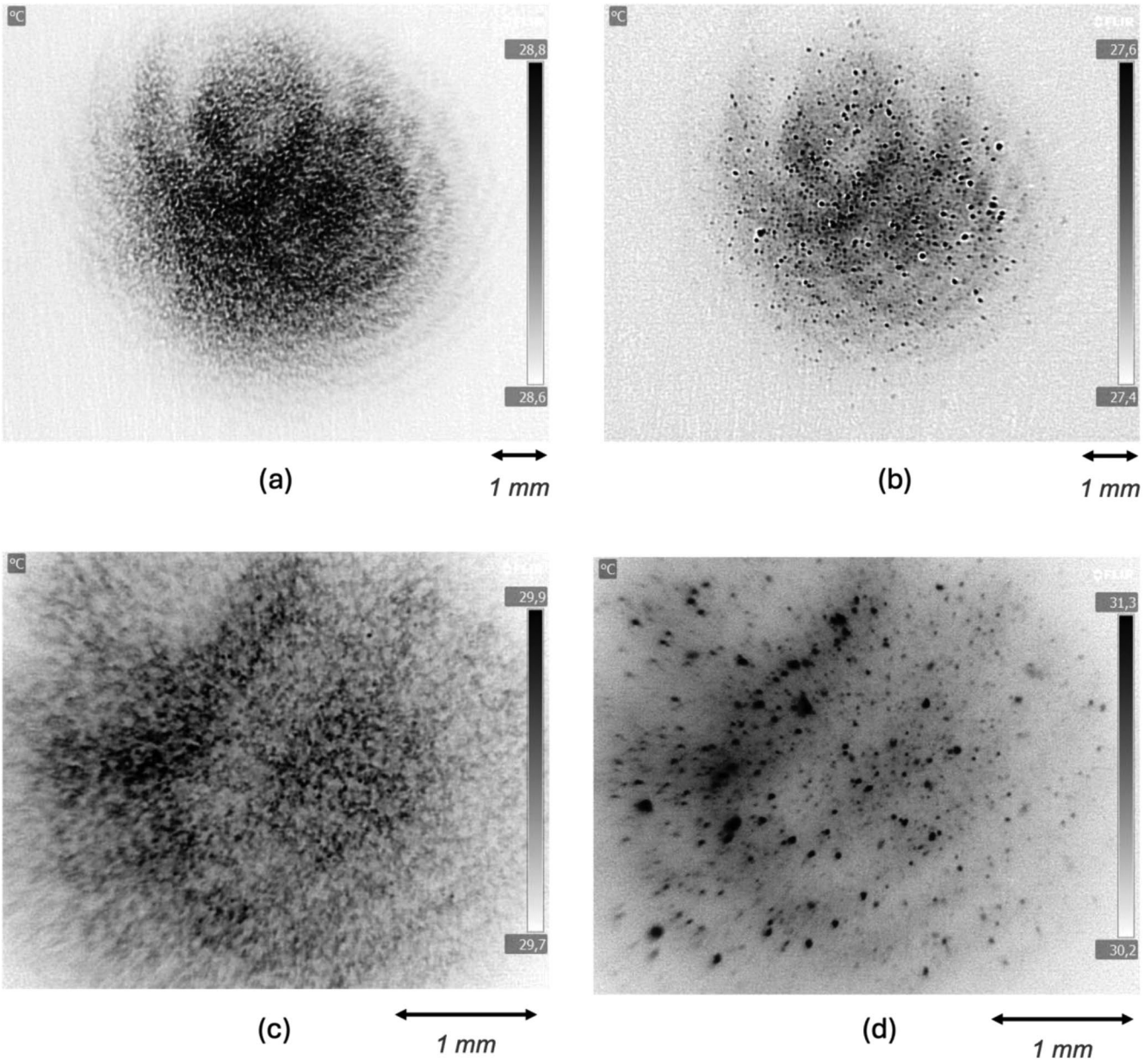

FIGURE 9 | Thermogram obtained with the PLMT technique of CNTs nanocomposites with sample A (a, c) and B (b, d). The different magnifications in the images correspond to the PLMT setup with (a, b) and without (c, d) the extension rings.

images where the background is not uniform, was applied followed by a median filter to reduce noise by replacing each pixel value with the median of the neighboring pixels. An example of the processed IR thermogram for PT and PLMT is shown in Figure 11. Subsequently, the data were analyzed with a custom Python code to retrieve information on the average distance between particles, the minimum, maximum, and average particle diameter. Also, the signal-to-noise ratio (black pixels = 255; white pixels = 0) was evaluated by dividing the signal from the NPs by the mean gray value of the selected ROI. Further, the processing time was determined with the FLIR research IR software by calculating the time needed for the specimen to cool down to its thermal equilibrium after the thermal stimuli (Figure 12). Finally, the thermal penetration depth was evaluated according to the pulsed excitation solution of the heat diffusion equation for the two heat stimuli [41, 42]. The quantitative data obtained from the image analysis were then used to compare the PT and PLMT setups and reported in Table 5. A reliability and repeatability study on the PLMT technique is shown in Table 6, where five different regions within the same sample B (reliability column) and five consecutive laser shots at 2 Hz on the same spot of sample B (repeatability column) are processed.

4 | Discussion

The discrimination of carbon-based NPs within epoxy employing a thermographic approach is based on the different thermal properties between the two phases (as reported in Table 2). Specifically, in Figure 9, the black spots correspond to a phase at a higher temperature during the thermal excitation with respect to the environment, such as in this case of CNTs and epoxy resin. Indeed, the ability of a material to rise in temperature is

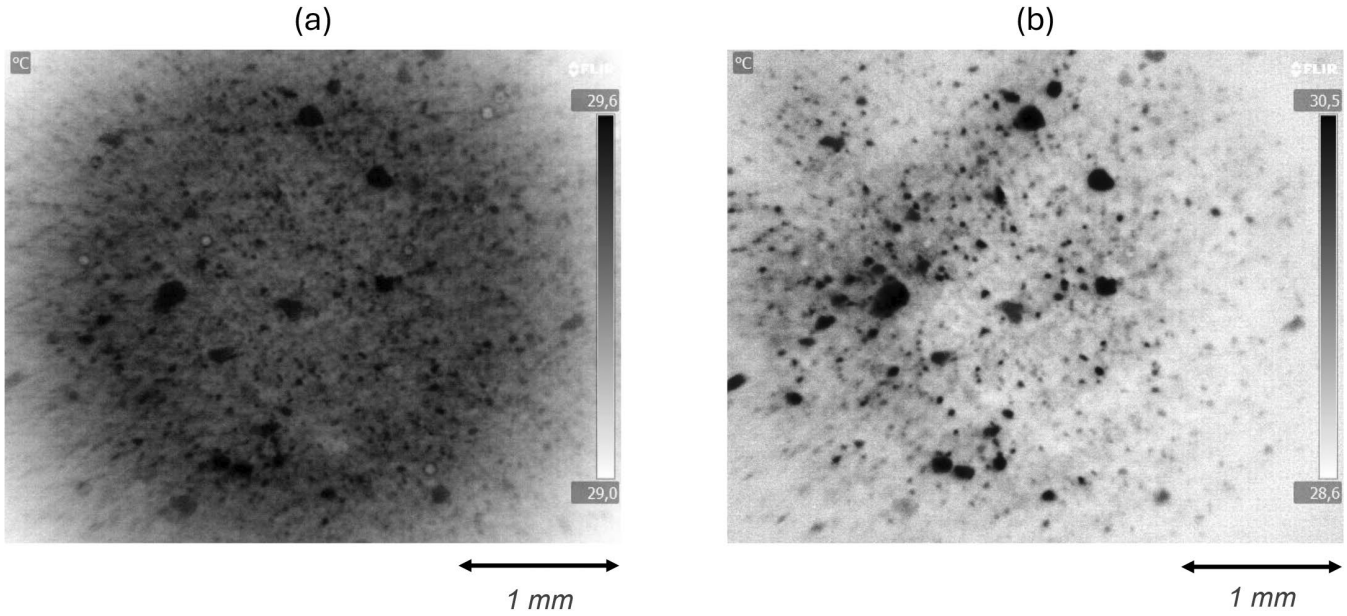

FIGURE 10 | CNTs nanocomposite (sample B) analyzed with the flash-based (PT) (a) and laser-based (PLMT) (b) thermography technique for the NPs dispersion assessment. The images both refer to the same region of interest.

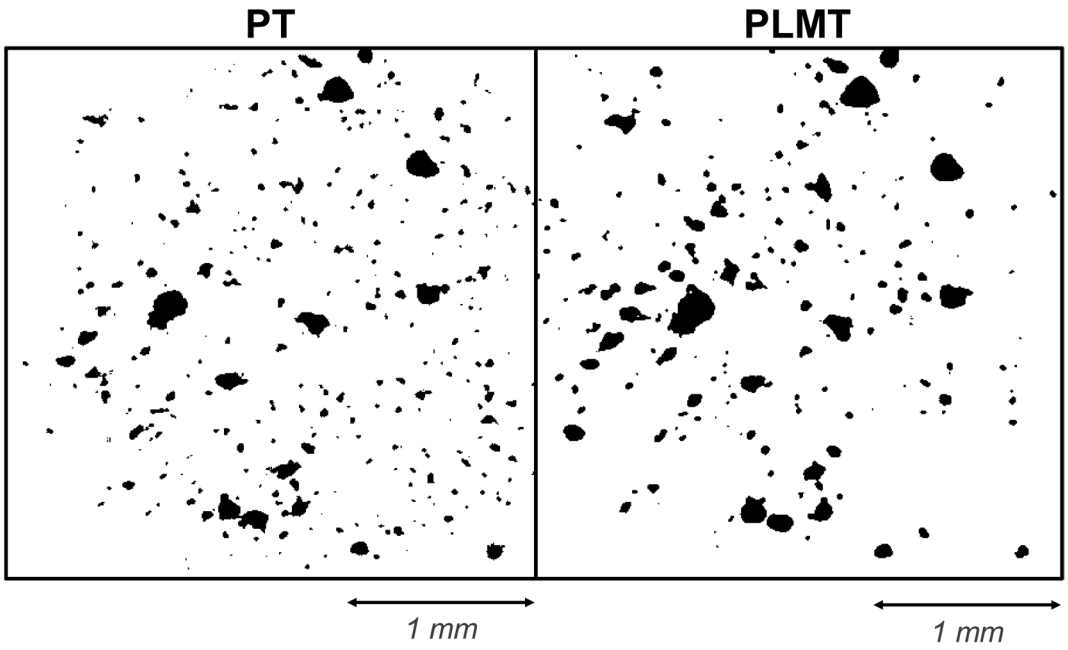

FIGURE 11 | Processed PT (on the left) and PLMT (on the right) thermograms referred to the same ROI of sample B used for the quantitative evaluation.

given by the coefficient of thermal diffusivity α, which is nearly two orders of magnitude higher for CNTs aggregates than epoxy. Therefore, CNTs bundles will tend to heat up faster and reach higher temperatures with respect to the surrounding material. Also, since the interface between different phases could be a region of discontinuity, thus a thermal barrier for diffusion, the heat encapsulated by the aggregates will be confined and hardly diffused through the less conductive resin. Consequently, throughout the transient thermal phenomena (heating/cooling), the regions at higher thermal diffusivity will have a temperature spread compared to the surrounding regions with lower thermal diffusivity. This was already demonstrated at a more macroscopic level by analyzing the overall thermal response of NCs at different filling percentages of CNTs. Increasing the filling percentage of NPs, a higher NC thermal diffusivity is expected, leading to a higher mean temperature through the heating/cooling transient [32]. In this work, thanks to the higher energetic and geometric resolution achieved with the proposed PLMT, the mechanism can be observed at the micro-scale.

Table 6 summarizes the main indices for evaluating the robustness of the proposed PLMT techniques. The relative standard deviation is generally low for all the calculated indices ($<7\%$) for the repeatability study, with the shots in the same region, except for the particle count and the signal-to-noise ratio reaching respectively 16.7% and 13.6%. Both deviations

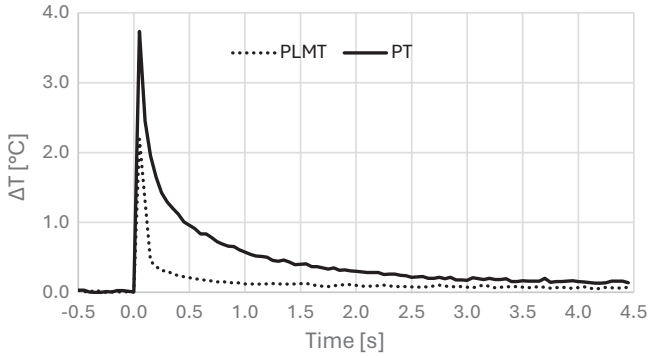

FIGURE 12 | Cooling transient comparison for PT and PLMT techniques for the Sample B.

TABLE 5 | Quantitative evaluation comparison for the PT and PLMT techniques.

	PT		PLMT	
	Mean	Relative std. dev. (%)	Mean	Relative std. dev. (%)
Signal to noise ratio (/)	1.3	1	2.7	6
Processing time (s)	4.2	0	1.2	0
No. of particles (/)	286.5	12.6	186	5.3
Average distance (mm)	79	2.7	105.9	0.2
Average diameter (mm)	26.6	14.1	40.6	3.0
Min. diameter (mm)	6.8	0.0	6.8	0.0
Max. diameter (mm)	160.8	20.8	193.1	19.5
Thermal penetration depth (mm)	88	0	0.2	0

are a consequence of the sample heating during the laser's multiple shots. The phenomenon is due to the laser repetition rate (2 Hz) being quicker than the cooling transient of the sample (cooling transient > 0.5 s, see Figure 12). This leads to heat accumulation, thus sample heating, which reduces the temperature spread between the NPs and resin. It decreases the signal-to-noise ratio and, in turn, the ability to accurately discriminate the exact number of particles. On the contrary, for the reliability study, where the shots were acquired in different spots on the sample, the over-heating is not taking place. Indeed, the signal-to-noise ratio is higher, and the relative standard deviation is smaller (9%) than in the repeatability study. However, in this case both the maximum diameter and number of particles indices show a standard deviation larger than 20%, which is attributed to inferential statistics of analyzing different areas of the sample. Finally, the PLMT robustness is further confirmed by the result with the maximum dimension of particles detected, which falls in the same range as that found in the SEM acquisition (around 200 μm, see Figure 3).

TABLE 6 | Repeatability analyses for the PLMT techniques processing images obtained by pulsing 5 consecutive laser shots on the same spot; Statistical analyses for the PLMT techniques processing images obtained in 5 different regions of the same sample.

	Repeatability: shots on the same region		Reliability: shots on the same sample	
PLMT	Mean	Relative std. dev. (%)	Mean	Relative std. dev. (%)
Signal to noise ratio (/)	2.4	13.6	2.7	9
Processing time (s)	1.2	0	1.2	0
N° of particles (/)	246.8	16.7	175.0	23.7
Average distance (μm)	91.7	6.4	107.8	9.1
Average diameter (μm)	34.8	1.4	38.8	8.5
Min. diameter (μm)	6.8	0	6.8	0
Max. diameter (μm)	197.3	1	217.3	24.6
Thermal penetration depth (μm)	0.2	0	0.2	0

In Table 5, a quantitative comparison of the main indicators of performance of the PT and PLMT techniques is shown. Thanks to the high geometric resolution of the employed IR lenses equipped with extension rings (6 μm/px) and the applied image processing algorithms, it is shown that the minimum detectable diameter of CNT clusters for both techniques is equal to 6.8 μm. Further, the considerable difference in energetic resolution for PT and PLMT, as seen from the signal-to-noise ratio being 1.3 and 2.7 respectively, is a direct consequence of the corresponding high spread in the thermal

penetration depth. Indeed, the greater penetration depth of PT allows for the detection of a higher number of particles compared to PLMT (287 vs. 186); however, this also negatively affects the signal-to-noise ratio, as multiple layers of particles deeper within the material's volume are compressed into a two-dimensional image. The depth of analysis was estimated (~88 μm and ~200 nm for PT and PLMT respectively) by applying the equation for the thermal diffusion length in case of impulse excitation:

$$L = \sqrt{\pi \alpha \tau}$$

where τ is the time scale of the corresponding heat stimuli [42]. Specifically, the quicker pulse width of the laser compared to the flash lamp (~9 ns vs. ~6 ms, respectively) has a significant impact on the energetic resolution achieved in the acquired IR thermogram. This results in significantly better-contrasted and more uniform images for PLMT, making the phase contours in the sample B inspection more evident (see Figure 10).

Another advantage of the short pulses for PLMT lies in the fact that the energy is delivered in a narrow time window, thus without inducing any permanent damage to the samples' surface. Clearly, as demonstrated in the surface degradation study (Section 3.1) on the pure epoxy sample, above a certain threshold of energy (150 mJ) the material starts to get damaged anyway. The appearing spots at higher temperatures (black spots) in Figure 7 indicate the formation of a phase with a different thermal response from the intact material, namely at higher conductivity. Presumably, this is related to combustion reactions at the micro-scale with the consequent formation of carbonaceous species (e.g., carbon black) at the surface and sub-surface of the material due to thermal degradation. Studying the type of damage that occurred is out of the scope of the present work.

Both PT and PLMT techniques are to be considered superficial analysis, as they are not able to operate in the bulk of the considered specimens, whose thickness is 3 mm. However, PLMT could be effectively employed as a complementary investigation to SEM, as they both operate in the same range of depth inspection, being in SEM 1–10 nm to 10–500 nm for secondary and backscattered electrons respectively. Consequently, PLMT could be employed to provide an overall indication of particle distribution across a larger area of the sample, offering a cost-effective, fast, and straightforward approach, which can then be complemented by a more detailed investigation using the more resource-intensive SEM inspection.

In this manner, the current PLMT setup could be easily employed in industrial applications. This would be possible thanks to the relatively large stand-off distance (both with and without extension rings), which is enough to permit the reflection mode inspection. Indeed, both sides of the parts to be inspected are often not accessible for in-line quality control. Moreover, being the pulse shot time, the injected energy, and the laser spot relatively small (9 ns, 112 mJ, and 7.4 mm respectively), the cooling transient is limited to only 1.2 s (see Figure 12). Therefore, only a small portion of the surface is heated and framed in the IR camera FOV within the employed lenses (see Figure 4). This allows for multiple acquisitions along the surface without excessive heating of the specimen and consequent loss of thermal contrast. It provides an additional advantage regarding PT analysis, as a significant portion of the energy from the flash lamp is dispersed across the entire sample surface, which is considerably larger than the IR camera's FOV (see Figure 6). This results in a greater temperature rise and a longer thermalization time, thereby limiting the possibility of multiple consecutive acquisitions. That is, in PLMT, the material to be investigated could be placed on a motorized support to raster scan the whole surface. This represents an interesting outlook for the industrial field. The acquired thermograms along the entire part could be post-processed by means of optimized dedicated machine learning algorithms to reconstruct the overall particles dispersion pattern (e.g., photothermal super-resolution reconstruction and other post-processing techniques [43–45]). Following an initial investment for the IR camera and a 5-axis robot arm, curved parts would also be feasible for the inspection.

The new setup brought significant improvements to previous scientific works, where NPs dispersion levels of high filling content of graphene-based epoxy NCs, ranging from 2.5%$_{wt}$ to 40%$_{wt}$, were analyzed by PT reaching a spatial resolution of 20 μm/pxs [30, 31]. Indeed, within the proposed technique a resolution as low as 6 μm/pxs was achieved, allowing for cluster determination in low-filling content (0.5%$_{wt}$ and 1%$_{wt}$) NCs. However, it is seen that with the proposed PLMT technique, NPs dispersion assessment is effective only when there is a high difference in thermal diffusivity between filler and matrix. Therefore, new parameters should be considered to expand the range of possible characterizations materials. In particular, the effect of the pulse duration and the wavelength on the penetration depth and signal-to-noise ratio of the laser should be studied, as well as the application of the PLMT on different class of NCs.

5 | Conclusion

The proposed innovative non-destructive pulsed laser micro thermography (PLMT) technique was successful in detecting and assessing the dispersion level of aggregates in epoxy resin filled with CNTs at 0.5%$_{wt}$ and 1%$_{wt}$. Specifically, the use of a nanosecond laser-based pulsed source for active thermography led to an improved energetic resolution of the acquired IR images compared to classical flash-based setups. This, by taking advantage of the different thermal responses between the carbon-based filler and the polymeric matrix, resulted in more defined and contrasted images at the contours of the different phases in the material, simplifying the discrimination of NP aggregates. Also, the equipment of the IR camera with a macro lens and extension rings in the experimental setup resulted in a geometric resolution of the IR frames of 6 μm/pixel. CNTs clusters with dimensions as low as 6.8 μm were identified with the proposed technique after images post-processing analysis. Further, the employed PLMT works in reflection mode, meaning that only one side of the component needs to be accessible during the process. By integrating the inspection method with a robotized manipulator and by using AI image processing

software, this approach would enable fast, remote, and detailed in-line quality control of large NC parts.

Author Contributions

Nicola Montinaro: conceptualization, methodology, investigation, writing – review and editing. **Guglielmo Marchesa:** investigation, data curation, formal analysis, visualization, and writing – original draft. **Donatella Cerniglia:** validation and resources. **Antonio Pantano:** validation and supervision.

Conflicts of Interest

The authors declare no conflicts of interest.

Data Availability Statement

The raw infrared images acquired during the experimental activities and the python code used for data analysis of the processed images are available at the linked repository (DOI: 10.17632/t3rhwyg75c.1): https://data.mendeley.com/datasets/t3rhwyg75c/1.

References

1. M. Zaccone, A. Frache, L. Torre, I. Armentano, and M. Monti, "Effect of Filler Morphology on the Electrical and Thermal Conductivity of Pp/Carbon-Based Nanocomposites," *Journal of Composites Science* 5, no. 8 (2021): 196.

2. D. Bellisario, F. Quadrini, L. Santo, N. Montinaro, M. Fustaino, and A. Pantano, "Hybrid Nanocomposites With Ultra-Low Filling Content by Nano-Coating Fragmentation," *Polymer-Plastics Technology and Materials* 61, no. 1 (2022): 41–55, https://doi.org/10.1080/25740881.2021.1948060.

3. S. Dabees, V. Tirth, A. Mohamed, and B. M. Kamel, "Wear Performance and Mechanical Properties of MWCNT/HDPE Nanocomposites for Gearing Applications," *Journal of Materials Research and Technology* 12 (2021): 2476–2488, https://doi.org/10.1016/j.jmrt.2020.09.129.

4. S. Clifton, B. H. S. Thimmappa, R. Selvam, and B. Shivamurthy, "Polymer Nanocomposites for High-Velocity Impact Applications—A Review," *Composites Communications* 17 (2020): 72–86, https://doi.org/10.1016/j.coco.2019.11.013.

5. B. Fiedler, F. H. Gojny, M. H. G. Wichmann, M. C. M. Nolte, and K. Schulte, "Fundamental Aspects of Nano-Reinforced Composites," *Composites Science and Technology* 66, no. 16 (2006): 3115–3125, https://doi.org/10.1016/j.compscitech.2005.01.014.

6. M. H. Al-Saleh and U. Sundararaj, "Review of the Mechanical Properties of Carbon Nanofiber/Polymer Composites," *Composites Part A, Applied Science and Manufacturing* 42, no. 12 (2011): 2126–2142, https://doi.org/10.1016/j.compositesa.2011.08.005.

7. H. S. Khare and D. L. Burris, "A Quantitative Method for Measuring Nanocomposite Dispersion," *Polymer* 51, no. 3 (2010): 719–729, https://doi.org/10.1016/j.polymer.2009.12.031.

8. X. Fu, J. Wang, J. Ding, H. Wu, Y. Dong, and Y. Fu, "Quantitative Evaluation of Carbon Nanotube Dispersion Through Scanning Electron Microscopy Images," *Composites Science and Technology* 87 (2013): 170–173, https://doi.org/10.1016/j.compscitech.2013.08.014.

9. V. Levin, E. Morokov, Y. Petronyuk, et al., "Cluster Microstructure and Local Elasticity of Carbon-Epoxy Nanocomposites Studied by Impulse Acoustic Microscopy," *Polymer Engineering and Science* 57, no. 7 (2017): 697–702, https://doi.org/10.1002/pen.24608.

10. I. Artyukov, S. Bellucci, V. Kolesov, et al., "Studies of Fractal Microstructure in Nanocarbon Polymer Composites," *Polymers* 16, no. 10 (2024): 1354, https://doi.org/10.3390/polym16101354.

11. S. Zhang, L. Cheng, H. Wang, Y. Qiu, L. Yang, and X. Zhao, "Nonlinear Acoustic Response in Nanoparticle-Dielectric Systems and Nondestructive Assessment of Particle Agglomeration," *Colloids and Surfaces A: Physicochemical and Engineering Aspects* 692 (2024): 133969, https://doi.org/10.1016/j.colsurfa.2024.133969.

12. S. Kim, W. I. Lee, and C. H. Park, "Assessment of Carbon Nanotube Dispersion and Mechanical Property of Epoxy Nanocomposites by Curing Reaction Heat Measurement," *Journal of Reinforced Plastics and Composites* 35, no. 1 (2016): 71–80, https://doi.org/10.1177/0731684415613704.

13. F. J. Galindo-Rosales, P. Moldenaers, and J. Vermant, "Assessment of the Dispersion Quality in Polymer Nanocomposites by Rheological Methods," *Macromolecular Materials and Engineering* 296, no. 3–4 (2011): 331–340, https://doi.org/10.1002/mame.201000345.

14. F. Mazaheri Karvandian, D. M. Phillips, E. Myzeqari, and P. Hubert, "Chemo-Rheological and Quantitative Dispersion Analysis of Mass-Produced Graphene-Unsaturated Polyester Based Nanocomposites," *Polymer Composites* 45, no. 11 (2024): 10290–10300, https://doi.org/10.1002/pc.28473.

15. N. Montinaro, D. Cerniglia, and G. Pitarresi, "Evaluation of Interlaminar Delaminations in Titanium-Graphite Fibre Metal Laminates by Infrared NDT Techniques," *NDT and E International* 98 (2018): 134–146, https://doi.org/10.1016/j.ndteint.2018.05.004.

16. K. Chatterjee, S. Tuli, S. G. Pickering, and D. P. Almond, "A Comparison of the Pulsed, Lock-In and Frequency Modulated Thermography Nondestructive Evaluation Techniques," *NDT and E International* 44, no. 7 (2011): 655–667, https://doi.org/10.1016/j.ndteint.2011.06.008.

17. A. G. Divin, S. v. Karpov, Y. A. Zakharov, et al., "Using Laser Point Scanning Thermography for Quality Monitoring of Products Made of Composite Materials," *Engineering Technologies and Systems* 34, no. 1 (2024): 145–163, https://doi.org/10.15507/2658-4123.034.202401.145-163.

18. T. Aujeszky, G. Korres, and M. Eid, "Measurement-Based Thermal Modeling Using Laser Thermography," *IEEE Transactions on Instrumentation and Measurement* 67, no. 6 (2018): 1359–1369, https://doi.org/10.1109/TIM.2017.2785138.

19. A. Alasli, R. Fujita, and H. Nagano, "Thermophysical Properties Mapping of Composites by Lock-In Thermography: Applications on Carbon Fiber Reinforced Plastics," *International Journal of Thermophysics* 43, no. 12 (2022): 176, https://doi.org/10.1007/s10765-022-03109-7.

20. J. A. Aguilar-Jimenez, N. W. Pech-May, I. Y. Forero-Sandoval, J. J. Alvarado-Gil, F. Cervantes-Alvarez, and F. Cervantes-Alvarez, "Thermal Characterization of Polyester Resin Composites Loaded With Graphite Rod-Like Inclusions Using Front-Face Laser-Flash Thermography," *Applied Composite Materials* 32 (2025): 937–954, https://doi.org/10.1007/s10443-025-10313-9.

21. B. Hyla, M. Sobczak, P. Synaszko, and J. Roemer, "Laser Spot Thermography and Pulse Thermography-Comparison of Performance for Non-Destructive Testing of Composite Structures," *International Journal of Multiphysics* 17 (2023): 91–104, https://doi.org/10.21152/1750-9548.17.1.91.

22. Z. He, H. Wang, Y. He, et al., "Joint Scanning Laser Thermography Defect Detection Method for Carbon Fiber Reinforced Polymer," *IEEE Sensors Journal* 20, no. 1 (2020): 328–336, https://doi.org/10.1109/JSEN.2019.2941077.

23. H. Liu, L. Tinsley, K. Deng, et al., "A Fiber-Guided Motorized Rotation Laser Scanning Thermography Technique for Impact Damage Crack Inspection in Composites," *IEEE Transactions on Industrial Electronics* 71, no. 3 (2024): 3163–3172, https://doi.org/10.1109/TIE.2023.3265034.

24. C. Mineo, N. Montinaro, M. Fustaino, A. Pantano, and D. Cerniglia, "Fine Alignment of Thermographic Images for Robotic Inspection of Parts With Complex Geometries," *Sensors* 22, no. 16 (2022): 6267, https://doi.org/10.3390/s22166267.

25. L. Santoro and R. Sesana, "A Pilot Study Using Flying Spot Laser Thermography and Signal Reconstruction," *Optics and Lasers in Engineering* 188 (2025): 108901, https://doi.org/10.1016/j.optlaseng.2025.108901.

26. R. Almadhoun, T. Taha, L. Seneviratne, J. Dias, and G. Cai, "A Survey on Inspecting Structures Using Robotic Systems," in *International Journal of Advanced Robotic Systems*, vol. 13 (SAGE Publications Inc., 2016), 1–18, https://doi.org/10.1177/1729881416663664.

27. M. Gresil, Z. Wang, Q. A. Poutrel, and C. Soutis, "Thermal Diffusivity Mapping of Graphene Based Polymer Nanocomposites," *Scientific Reports* 7, no. 1 (2017): 5536, https://doi.org/10.1038/s41598-017-05866-0.

28. A. Manta, M. Gresil, and C. Soutis, "Infrared Thermography for Void Mapping of a Graphene/Epoxy Composite and Its Full-Field Thermal Simulation," *Fatigue and Fracture of Engineering Materials and Structures* 42, no. 7 (2019): 1441–1453, https://doi.org/10.1111/ffe.12980.

29. G. Mirabello, L. Steinmetz, C. Geers, et al., "Quantification of Nanoparticles' Concentration Inside Polymer Films Using Lock-In Thermography," *Nanoscale Advances* 5, no. 11 (2023): 2963–2972, https://doi.org/10.1039/d3na00091e.

30. A. Ashraf, N. Jani, F. Farmer, and J. K. Lynch-Branzoi, "Non-Destructive Investigation of Dispersion, Bonding, and Thermal Properties of Emerging Polymer Nanocomposites Using Close-Up Lens Assisted Infrared Thermography," *MRS Advances* 5, no. 14–15 (2020): 735–742, https://doi.org/10.1557/adv.2020.121.

31. M. A. Rahman, M. M. Rahman, and A. Ashraf, "Automatic Dispersion, Defect, Curing, and Thermal Characteristics Determination of Polymer Composites Using Micro-Scale Infrared Thermography and Machine Learning Algorithm," *Scientific Reports* 13, no. 1 (2023): 2787, https://doi.org/10.1038/s41598-023-29270-z.

32. A. Pantano, N. Montinaro, D. Cerniglia, et al., "Novel Non-Destructive Evaluation Technique for the Detection of Poor Dispersion of Carbon Nanotubes in Nanocomposites," *Composites Part B: Engineering* 163 (2019): 52–58, https://doi.org/10.1016/j.compositesb.2018.10.097.

33. N. Montinaro, M. Fustaino, D. Bellisario, F. Quadrini, L. Santo, and A. Pantano, "Testing the Dispersion of Nanoparticles in a Nanocomposite With an Ultra-Low Fill Content Using a Novel Non-Destructive Evaluation Technique," *Materials* 15, no. 3 (2022): 1208, https://doi.org/10.3390/ma15031208.

34. N. Montinaro, M. Fustaino, and A. Pantano, "Carbon Nanotubes Dispersion Assessment in Nanocomposites by Means of a Pulsed Thermographic Approach," *Materials* 13, no. 24 (2020): 1–13, https://doi.org/10.3390/ma13245649.

35. K. W. Garrett and H. M. Rosenberg, "The Thermal Conductivity of Epoxy-Resin / Powder Composite Materials the Thermal Conductivity of Epoxy-Resin /Powder Composite Materials," *Journal of Physics D: Applied Physics* 7 (1974): 1247, http://iopscience.iop.org/0022-3727/7/9/311.

36. K. Kadoya, N. Matsunaga, and A. Nagashima, "Viscosity and Thermal Conductivity of Dry Air in the Gaseous Phase," *Journal of Physical and Chemical Reference Data* 14, no. 4 (1985): 947–970, https://doi.org/10.1063/1.555744.

37. A. E. Aliev, M. H. Lima, E. M. Silverman, and R. H. Baughman, "Thermal Conductivity of Multi-Walled Carbon Nanotube Sheets: Radiation Losses and Quenching of Phonon Modes," *Nanotechnology* 21, no. 3 (2010): 035709, https://doi.org/10.1088/0957-4484/21/3/035709.

38. Y. Ma, C. Xin, W. Zhang, and G. Jin, "Experimental Study of Plasma Plume Analysis of Long Pulse Laser Irradiates Cfrp and Gfrp Composite Materials," *Crystals* 11, no. 5 (2021): 545, https://doi.org/10.3390/cryst11050545.

39. M. Devi, H. Wang, S. Moon, S. Sharma, and V. Strauss, "Laser-Carbonization – A Powerful Tool for Micro-Fabrication of Patterned Electronic Carbons," *Advanced Materials* 35, no. 38 (2023): 2211054, https://doi.org/10.1002/adma.202211054.

40. J. Sauvola and M. Pietikak, "Adaptive Document Image Binarization," *Pattern Recognition* 33 (2000): 225–236, https://doi.org/10.1016/S0031-3203(99)00055-2.

41. N. Rajic, "Non-Destructive Evaluation (NDE) of Aerospace Composites: Flaw Characterisation," in *Non-Destructive Evaluation (NDE) of Polymer Matrix Composites: Techniques and Applications* (Wood Publishing, 2013), 335–366, https://doi.org/10.1533/9780857093554.3.335.

42. S.-S. Wellershoff, J. Hohlfeld, J. Güdde, and E. Matthias, "The Role of Electron–Phonon Coupling in Femtosecond Laser Damage of Metals," *Applied Physics A: Materials Science and Processing* 69, no. S1 (1999): S99–S107, https://doi.org/10.1007/s003399900305.

43. L. Presotto, M. Marini, G. Chirico, et al., "Super-Resolution Photothermal Imaging at the Microscale by Model-Based Image Reconstruction," *Advanced Intelligent Systems* 6, no. 1 (2024): 2300510, https://doi.org/10.1002/aisy.202300510.

44. J. Yin, L. Lan, Y. Zhang, et al., "Nanosecond-Resolution Photothermal Dynamic Imaging via MHZ Digitization and Match Filtering," *Nature Communications* 12, no. 1 (2021): 7097, https://doi.org/10.1038/s41467-021-27362-w.

45. V. Vavilov, A. Chulkov, V. Shiryaev, and D. Kladov, "A Novel Reference-Free Technique for Processing One-Sided Thermal NDT Results in the Time Domain," *NDT and E International* 143 (2024): 103032, https://doi.org/10.1016/j.ndteint.2023.103032.